A single particle model to simulate the dynamics of entangled polymer melts

P. Kindt[a)] and W. J. Briels[b)]

Computational Biophysics, Department of Science and Technology, University of Twente, P.O. Box 217, 7500 AE Enschede, The Netherlands

We present a computer simulation model of polymer melts representing each chain as one single particle. Besides the position coordinate of each particle, we introduce a parameter n_{ij} for each pair of particles i and j within a specified distance from each other. These numbers, called entanglement numbers, describe the deviation of the system of ignored coordinates from its equilibrium state for the given configuration of the centers of mass of the polymers. The deviations of the entanglement numbers from their equilibrium values give rise to transient forces, which, together with the conservative forces derived from the potential of mean force, govern the displacements of the particles. We have applied our model to a melt of $C_{800}H_{1602}$ chains at 450 K and have found good agreement with experiments and more detailed simulations. Properties addressed in this paper are radial distribution functions, dynamic structure factors, and linear as well as nonlinear rheological properties. © 2007 American Institute of Physics. [DOI: 10.1063/1.2780151]

I. INTRODUCTION

Experimentalists as well as theoreticians put great effort in predicting the dynamical properties of polymeric materials if only because flow behavior of polymer melts is of great importance in industrial applications. Rheological experiments reveal complicated molecular weight dependencies of viscosities and diffusion coefficients. Polymers combine a large zero shear viscosity with strong shear thinning at high shear rates. Neutron-spin-echo spectroscopy measurements indicate that several relaxation mechanisms govern the decay of stresses over a broad time window, associated with many different length scales.[1–3] The two best known theories describing polymer melt dynamics are the Rouse model for short chains[4] and the reptation model for entangled chains.[5,6] The latter describes equilibrium and low shear rate properties of highly entangled melts very well, but misses important relaxation mechanisms to correctly describe moderately entangled melts and nonlinear rheological properties. Several successful extensions have been made to the original reptation model in order to incorporate mechanisms like (convective) constraint release (CCR/CR) and tube length fluctuations.[7–11]

Several types of computer simulations may be discerned in this field. First, there are simulations based on the atomistic structure of the chains, either by running atomistic molecular dynamics simulations directly[12,13] or by performing some kind of bottom-up coarse graining like in the Twentanglement model.[14] At present, these methods are incapable of simulating well entangled melts long enough to faithfully sample all characteristic relaxations, including the slowest ones. A second class of models includes the bond fluctuation model[15] and the Kremer-Grest model.[16] In both cases the polymers are represented by fully flexible chains of hard segments connected in such a way that bond crossings are prevented by repulsive forces between the segments. It has turned out to be difficult with these models to find unique sets of model parameters capable of describing a broad spectrum of properties of one and the same polymer melt. Their great merit, however, has been to provide a wealth of information about the scaling laws that govern the dynamics and rheology of polymer melts. A third class of models is the class of slip-link models based on a direct implementation of reptation concepts. In the model of Marrucci entanglements between chains are created and annihilated in the neighborhoods of chain ends in a three dimensional simulation, while in Likhtman's model only one chain is modeled in a fluctuating background represented by anchored springs with rings at their ends. Particularly, the last model is very attractive because of its simplicity and cheapness in terms of CPU consumption. Both models, however, will meet great difficulties in case they are to be extended to describe the rheology of block copolymers or colloid polymer mixtures, or, for example, viscoelastic phase separation kinetics.

In this work we aim for a polymer model, which is simple enough to allow for fast simulations and at the same time is versatile enough to be applicable in situations mentioned in the last sentence of the previous paragraph. An obvious candidate seems to be a model in which each polymer is represented by just one particle. The first to introduce a model like this were Murat *et al.*,[17] but they restricted themselves to describing the static properties of the melt, ignoring its entanglement driven dynamics. To cover entanglement effects, we introduce a time dependent pairwise "order parameter," which governs the friction felt by each chain and results in restoring elastic forces. We have tested the model for a polyethylene (PE) melt of $C_{800}H_{1602}$, both in

---

a)Electronic mail: kindt.peter@gmail.com
b)Electronic mail: w.j.briels@utwente.nl

127, 134901-1

equilibrium and in shear flow and have found good agreement in both cases with available experimental data.

This paper is structured as follows: Section II describes the construction of the model. Section III contains the static and dynamic equilibrium results of the new model. In Sec. IV transient and steady state shear flows are studied, followed by a discussion in Sec. V.

II. MODEL

A. Coarse graining

Coarse graining of polymers amounts to collecting a number of segments into a single particle. Depending on the degree of coarse graining, the particles exhibit much less structure than what occurs on the atomistic scale. For very high levels of coarse graining, the radial distribution function $g(r)$ approaches 1 for all values of r, indicating that there is no particle ordering on the coarse length scales. The correct $g(r)$ in these cases can only be achieved by the use of soft potentials, while harder potentials such as Dissipative Particle Dynamics (DPD) potentials or truncated Lennard-Jones potentials will fail.

Coarse graining polymer chains into single particles ultimately results in an effort to simulate a polymer melt as an ideal gas. Even the introduction of a large background friction in a Brownian dynamics simulation will fail for the following reason. Polymer melts have very large viscosities, $\eta \propto L^3$, with L as the length of the chain, while at the same time the diffusion coefficient D is also relatively large. As a result, $\eta D \propto L^6$.[6] Independent of the details of the potential, a Brownian dynamics simulation will yield $\eta D \propto L^0$. Either η or D will be too low, as will be shown in Sec. III. The origin of the atypical behavior of the polymer melts, of course, is to be found in the entanglements or topological constraints, giving rise to tubes within which the polymers reptate. Any single particle model successfully describing melt rheology must somehow incorporate the effects of entanglements.

B. Entanglements

During simulations of polymer melts using one of the multiparticle representations obeying the uncrossability constraint on the polymer chains, entanglements between chains appear and disappear continuously. Their effect on the dynamics of the polymers pervades through all time and length scales. In particular, their presence makes the dynamics of the internal degrees of freedom of the polymers almost equally slow as the movements of the centers of mass of the polymers. This lack of separation of time scales makes any attempt to simulate the movements of the centers of mass by means of a standard Brownian dynamics propagator, ignoring all internal degrees of freedom, a lost case. Instead, we propose to use a method introduced recently by van den Noort et al.,[18] in which the state of affairs of the ignored degrees of freedom is described by a small number of parameters.

When two unentangled polymers are fixed at a distance r, they will interpenetrate and relax to some equilibrium state depending on the distance. The overlap of polymers i and j will be described by a single parameter n_{ij} that may be considered to represent the number of "entanglements" between both polymers. On the Brownian time scale, the state of the system is then fully determined by N vectors $\mathbf{r}_i$ and $1/2N(N-1)$ entanglement numbers n_{ij}. The equilibrium probability density Ψ reads

$$\Psi(r^{3N}, n^{1/2N(N-1)})$$

$$\propto \exp\left\{-\frac{1}{k_B T}\left[A_c(r^{3N}) + \sum_{\langle i,j\rangle} \frac{1}{2}\alpha(n_{ij}-n_0(r_{ij}))^2\right]\right\}, \quad (1)$$

where k_B is Boltzmann's constant and T the temperature. A_c is the free energy of the ignored coordinates at the given configuration R^{3N} of the centers of mass of the polymers and $\Sigma_{\langle i,j\rangle}$ is used as a notation for a sum over all interacting particle pairs. The constant α determines the strength of the fluctuations in the number of entanglements around n_0. n_{ij} can take any value, both positive and negative, so that after integration over n_{ij} the coordinates are distributed according to the usual Boltzmann distribution. In other words, the static properties of the system are not altered by the introduction of the entanglements. The equilibrium number of entanglements $n_0(r_{ij})$ will be chosen, different from that in Ref. 18, where $n_0(r) \propto 1/r$ was used. In contrast to the resin particles studied in Ref. 18, polymers can fully overlap. In order to prevent entanglement numbers from being infinite in this case, we have chosen $n_0(r_{ij})$ as

$$n_0(r_{ij}) = \begin{cases} c(r_{ij}-r_c)^2: & r_{ij} < r_c \\ 0: & r_{ij} > r_c, \end{cases}$$

$$c = \frac{15}{2\pi r_c^5}, \quad (2)$$

where r_c is a cutoff radius, which should be several times the radius of gyration R_G. It is chosen to be 2.5 times R_G of the polymer. c can be chosen arbitrarily because αc^2 is the only relevant parameter. Here, c is used to normalize n_0.

The resulting displacement $d\mathbf{r}$ per time step dt may be derived[19] using the standard procedure for obtaining the Smoluchowski equation and reads

$$d\mathbf{r}_i = \Theta\sqrt{2k_B T dt/\xi_i} + \nabla_i\left(\frac{k_B T}{\xi_i}\right)dt + \frac{1}{\xi_i}\left\{-\nabla_i A_c(r^{3N})\right.$$

$$\left. - \sum_{j\neq i}\left(\alpha(n_0(r_{ij})-n_{ij})\frac{dn_o}{dr_{ij}}\frac{\mathbf{r}_{ij}}{r_{ij}}\right)\right\}dt. \quad (3)$$

The stochastic displacements, represented by the first term in the right hand side, are related by the fluctuation-dissipation theorem to the friction ξ_i discussed below; Θ is a random number with unit variance and zero mean. Equation (3) differs in two aspects from ordinary Brownian Dynamics (BD).

(1) The last term in Eq. (3) is an elastic term that drives the two particles to the distance that suits the current number of entanglements. It resembles the forces that entanglements create against deformation of the chain. This means that two approaching particles will repel

each other on average, whereas two separating particles will be pulled toward each other. (Note that dn_0/dr_{ij} is always negative.)

(2) The friction ξ_i differs from a constant background friction. Here, it depends on n_{ij} according to

$$\xi_i = \xi_e \sum_{j \neq i} n_{ij} n_0(r_{ij}), \tag{4}$$

with ξ_e as the friction per entanglement. The resistance against movement depends on the number of entanglements the chain has with its surrounding fellow chains.

Analogously to Eq. (3), the accompanying change in the number of entanglements on this Brownian time scale is

$$dn_{ij} = \Theta' \sqrt{2k_B T dt / \xi'} + \frac{\alpha}{\xi'}(n_0(r_{ij}) - n_{ij})dt. \tag{5}$$

ξ'/α can be viewed as the characteristic time it takes a pair of particles to relax to their equilibrium state. For polymers the longest relaxation time is the reptation time τ_d, so that Eq. (5) can be expressed as follows:

$$dn_{ij} = \Theta' \sqrt{2k_B T dt / \alpha \tau_d} + \frac{1}{\tau}(n_0(r_{ij}) - n_{ij})dt, \tag{6}$$

with $\tau \approx \tau_d$.

C. Compressibility

We have implemented the above equations of motion using soft Gaussian potentials, which were extrapolated from the work of Padding and Briels,[14]

$$A_c(r^{3N}) = \sum_{i,j} c_G \exp - r_{ij}^2 / b_0^2, \tag{7}$$

with the potential strength c_G decreasing and the Gaussian width b_0 increasing with the level of coarse graining. The results in equilibrium were promising, but the model failed under shear. In equilibrium there is no driving force for the particles to form clusters and the thermal fluctuations are capable of creating the appropriate mass distribution. In shear flow, however, the soft pairwise potential allows the particles to group together and thus to minimize the entanglement stresses. At the origin of this problem is the fact that the coarse system with soft pair potentials does not have the right compressibility κ_T.

Introducing the correct compressibility to compensate for the missing constraint of a constant local monomer density is not straightforward in mesoscopic simulations. The most widely used mesoscopic force fields, such as DPD or truncated Lennard-Jones potentials, can only achieve the correct compressibility at the expense of introducing unphysical, long ranged order. Furthermore, the large forces resulting from these potentials incorrectly influence the dynamics of the particles and lower the possible time step. The cause of all these problems must be the fact that the free energy $A_c(r^{3N})$ in Eq. (3) cannot be well represented by a sum of pair contributions and that many-body terms must be included. An elegant way of doing this has been devised by Pagonabarraga and Frenkel[20,21] in the framework of DPD,

and was called Multiparticle Dissipative Particle Dynamics (MDPD) by Trofimov et al.[22] Inspired by this work, we derive in the Appendix the conservative force field used in this paper by Taylor expanding the free energy of the eliminated coordinates in small deviations of the density field around the homogeneous state. Our result for the conservative force $\mathbf{F}_{ci}$ is

$$\mathbf{F}_{ci} = -\nabla_i A_c[\rho] = -\frac{1}{\rho^3 \kappa_T} \sum_{j=1}^{N} (\Delta_j + \Delta_i)\nabla_i \omega(r_{ij}). \tag{8}$$

Here, ρ is the macroscopic number density of chains and Δ_i is the excess local density around i, calculated by summing over the neighboring particles j with normalized weight functions $\omega(r_{ij})$ [Eq. (A3)] κ_T is the isothermal compressibility.

For convenience, the range of the weight function is chosen equal to that of n_0, i.e., 2.5 times the radius of gyration R_G of the polymer. This is somewhat on the small side since part of the monomer-monomer interactions will take place at larger distances. The limiting factor here is the number of particles within the cutoff volume, which should not grow too large in view of the CPU and random access memory consumptions. Let L be the number of segments in a chain; then, the number of particles N_j that interact with i scales as

$$\langle N_j \rangle = \frac{4}{3}\pi r_c^3 \rho \propto L^{3/2} L^{-1} = L^{1/2}, \tag{9}$$

where we have made use of random walk statistics for the scaling of the size of the polymer. For a relatively short PE chain (11 kg/mol) and $r_c = 2.5 R_G$, this already reaches values of the order of 10^2, where, e.g., the DPD value is about 10^1. Another restriction on the weight function is that it has to be monotonously decreasing, with a nonzero derivative at the origin. Without this restriction, the very small repulsive forces at short distances do not prevent the formation of lattice structures with several particles per site at high pressures[22] or in shear. A Gaussian weight function, best describing the density distribution of a polymer, can thus not be used. In order to give weight to as many particles as possible within a given cutoff and to have a nonzero derivative at the origin, a linear function is used,

$$\omega(r_{ij}) = \begin{cases} \dfrac{3}{\pi r_c^4}(r_c - r_{ij}): & r_{ij} < r_c \\ \\ 0: & r_{ij} > r_c. \end{cases} \tag{10}$$

This way of implementing the conservative force minimizes the local structure and still allows two particles to fully overlap without a large penalty in the free energy.

III. EQUILIBRIUM RESULTS

A. Simulation setup

Polyethylene is chosen as our test system since it has been studied experimentally[23] and by simulations[24–26] at the same temperature (450 K) and for chain lengths that are within the reach of the proposed one-particle model. The entanglement mass of PE is about 1.7 kg/mol found both in simulations[26] and in neutron-spin-echo experiments.[27] In or-

TABLE I. The input parameters of the model for $C_{800}H_{1602}$ PE at 450 K. κ_T is taken from Ref. 46 as an average value of hydrocarbons at 450 K, R_G and τ_d from Ref. 24, and the mass density ρ_M from Pearson *et al.* (Ref. 23). α and ξ_e are fitted to obtain the correct diffusion and viscosity.

Parameter	Value	Unit
ρ_M	761	kg/m^3
κ_T	1.5×10^{-9}	Pa^{-1}
R_G	4.64	nm
τ_d	1687	ns
dt	0.05	ns
α	6.21	aJ
$\xi_e/\rho k_B T$	3.2×10^{-15}	m s

der to be in the entangled regime and also close to the experimental chain lengths of Wischnewski *et al.* (12 kg/mol), we study $C_{800}H_{1602}$=11.2 kg/mol, corresponding to the B_{40} system of Padding and Briels.[24]

The input parameters of our system are listed in Table I. The mass density, radius of gyration, disentanglement time, and compressibility κ_T are taken from experiments and previous simulations. Only α, the entanglement interaction strength, and ξ_e, the friction per entanglement have been used as fitting parameters to realize the experimental diffusion coefficient and zero shear viscosity.

Due to the large number of pair interactions for each particle, about 250, we cannot restrict ourselves to systems as small as the 80 chain system of Ref. 24. In order to have box sizes larger than $2r_c$, we use boxes containing 800 particles. The time step is limited by the value of α/ξ_e and is $3 \times 10^{-5} \tau_d$=0.5 ns.

To get a feeling for the gain of computational speed provided by coarse graining, we have listed the values of Nf/dt for various simulation methods in Table II, which is a rough measure for the CPU consumption. The costs of all methods scale linearly with the number of particles and evidently inversely with the time step. f is a factor expressing the CPU time needed per particle per time step relative to that in a usual molecular dynamics (MD) simulation. For the Twentanglement method, f has been estimated by comparing runs with and without using the uncrossability constraint; for our new method, f=20 because the number of particles within r_c is about 20 times larger than in a normal MD simulation. From Table II it is clear that the profit with respect to all listed methods is huge (10^3-10^7).

All simulations discussed below started with a random configuration and a Boltzmann distribution for the entanglement numbers n_{ij}. Measurements started after equilibration

periods of at least τ_d. A typical CPU consumption of a production run is 24 h on a single Pentium 4 processor.

B. Structure

In order to test whether the thermodynamic equilibrium state is correctly reproduced by our model, several quantities were measured. The results for the system with entanglement interactions are presented in this and the next subsection. A comparison of the dynamical observables with those of an unentangled system is discussed in Sec. III D.

To investigate the distribution of the particles, the radial distribution function $g(r)$ and the structure factor $S(k)$,

$$S(k) = \frac{1}{N} \left\langle \sum_i^N \sum_j^N \exp(i\mathbf{k} \cdot [\mathbf{r}_i - \mathbf{r}_j]) \right\rangle, \quad (11)$$

were measured. Density fluctuations on infinitely large length scales are related to the compressibility κ_T by

$$S(k=0) = \rho k_B T \kappa_T. \quad (12)$$

This provides a means to test the proposed implementation of the compressibility by means of the potential in Eq. (8). In Fig. 1 $g(r)$ and $S(k)$ are plotted both for a system with and without entaglements. Both plots reveal no noticeable effect of the entanglements on the distribution of the particles. The radial distribution function exhibits a small correlation hole and virtually no local structure. Mavrantzas *et al.* have measured the $g(r)$ of C_{200} and C_{400} PE chains in atomistic Monte Carlo simulations and found the same correlation hole,[28] which shows that they almost have no excluded volume effect on the interchain level.

The compressibility of both systems, i.e., the one with and the one without entanglements, is equal to the input value in Eq. (8), showing that Eq. (8) provides a correct way to implement compressibility into coarse grained simulation methods. The quality of $g(r)$ lends credibility to the functional form and, in particular, the range of the weight function $\omega(r)$. Taking a broader range for $\omega(r)$ would have resulted in less structure, whereas a smaller range would have led to stronger excluded volume effects.

The distribution of the number of entanglements per pair of interacting particles is Gaussian, as follows directly from the Boltzmann distribution of Eq. (1). Equipartition can thus be used to measure the temperature of the system from the second moment.[18]

TABLE II. CPU consumption, N/dt, of different simulation methods of a melt of $C_{800}H_{1602}$ chains. Typical values for the time step and number of particles are given for atomistic MD, united atom MD, the Twentanglement model, and the new model in order to show the gain of coarse graining.

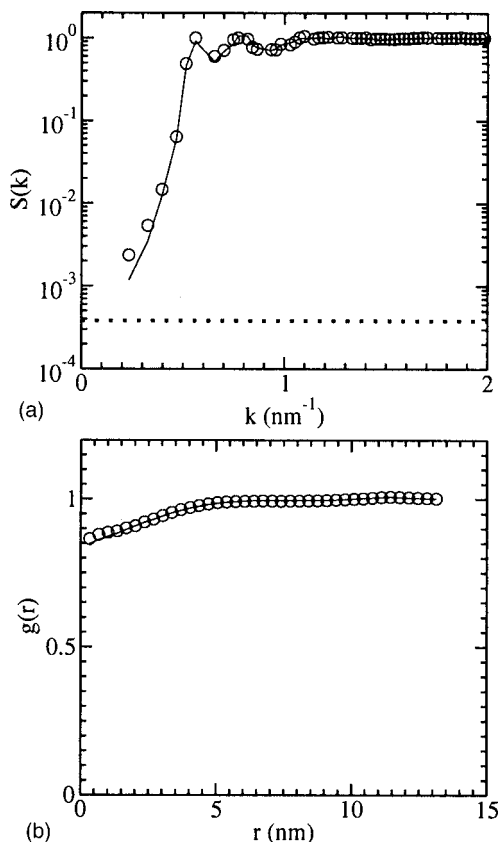| Method	N_{chains}	N	dt (s)	f	Nf/dt (s^{-1})	Acceleration
MD	80	192 160	0.5×10^{-15}	1	3.8×10^{20}	$1\times$
UA MD	80	64 000	2.0×10^{-15}	1	3.2×10^{19}	$10^1\times$
Twentanglement	80	3200	0.1×10^{-12}	10	3.2×10^{17}	$10^3\times$
New model	800	800	5.0×10^{-11}	20	3.2×10^{14}	$10^6\times$

(a)

(b)

FIG. 1. In (a) the structure factor is plotted, both for a system with (circles) and a system without (full line) entanglements. In the limit of $k \rightarrow 0$ the structure factor must be $s(k,0) = \rho k_B T \kappa_T = 3.8 \times 10^{-4}$, represented by the dotted line. Measuring low k values in simulations is limited by the box size, but for both systems the compressibility seems to be consistent with the input value. In (b) the radial distribution function $g(r)$ is plotted for both systems. The overlap between the centers of mass of the polymers is large as in a real melt. Both plots show that within a statistical error the structure is not changed by the introduction of entanglements.

$$\frac{1}{2}\alpha\langle(n_{ij} - n_0(r_{ij}))^2\rangle = \frac{1}{2}k_B T. \tag{13}$$

In normal BD simulations the temperature can only be measured by calculating the configurational temperature,[29] which is usually very noisy. Monitoring the entanglement temperature during equilibration and production runs provides a means to check that the time step is not chosen too large.

C. Dynamics

An important challenge in the field of polymer simulations is to simultaneously describe the dynamics and statics correctly. In the previous subsection we have shown that our model properly describes the structural properties of a PE melt. In this subsection we study its dynamic properties.

One of the more interesting and difficult to describe dynamic observables is the zero shear relaxation modulus,

$$G(t) = \frac{V}{k_B T}\langle\sigma_{\alpha\beta}(t)\sigma_{\alpha\beta}(0)\rangle, \quad \alpha \neq \beta, \tag{14}$$

with V as the volume of the simulation box and $\sigma_{\alpha\beta}$ the $\alpha\beta$ component of the stress tensor,
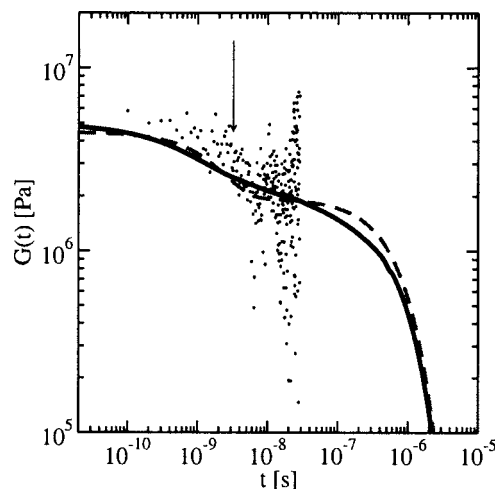

FIG. 2. The stress autocorrelation $G(t)$ of the entangled system (full line) compared with the results of the B_{40} system of the Twentanglement model of Padding and Briels (Ref. 24) (dots). The arrow indicates τ_e that they estimated for this system. Two relaxation times are visible in both the entangled system and the Twentanglement model in contrast to the unentangled system. The broken line represents a fit consisting of two exponents.

$$\sigma_{\alpha\beta} = \frac{1}{V}\sum_{i,j}(r_{i,\beta} - r_{j,\beta})F_{ij,\alpha}, \tag{15}$$

where $r_{i,\beta}$ is the β component of the position vector of particle i and $F_{ij,\alpha}$ is the α component of the force exerted by particle j on particle i. The zero shear viscosity η can be calculated using the Green-Kubo integral,

$$\eta = \int_0^\infty dt G(t). \tag{16}$$

Where other particle based simulations fail to reach the longest relaxation time for the present system, the new model easily allows for correlation times of a few τ_d and thus to perform the full integration of $G(t)$. With the chosen set of parameters, we find η to be 1.5 Pa s, where Pearson *et al.* measured $\eta = 2.09$ Pa s.

The shear relaxation modulus $G(t)$ describes the relaxation of stresses after a small step strain. It is plotted in Fig. 2 together with the simulation results of Padding and Briels.[24] Only the integral of this function has been fixed by adjusting the model parameters α and ξ_e. It is therefore interesting that the characteristics of $G(t)$ are very similar with both models. After an initial fast decay $G(t)$ reaches a plateau at $\tau_e = 5 \times 10^{-9}$ s in both cases. In the Twentanglement model the plateau results from long lived entanglements between different chains, while in the present one-particle model the slowly decaying transient entanglement forces are responsible. At times beyond 5×10^{-7} s, $G(t)$ decays exponentially with a characteristic time $\tau_d = 0.8 \times 10^{-6}$ s, which is only one-half the characteristic time occurring in Eq. (6). We leave the precise relation between τ and τ_d for future investigations.

The dashed line in Fig. 2 represents the results of a best fit of $G(t)$ with two exponentially decaying contributions. The largest characteristic time of the two was not involved in the fitting procedure, but fixed at the value of $=0.8 \times 10^{-6}$ s
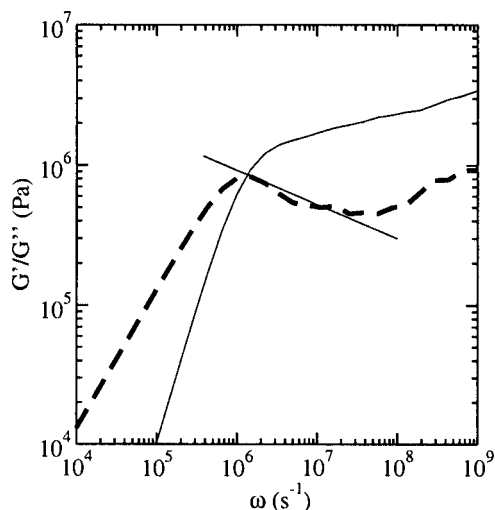
FIG. 3. The storage and loss moduli, $G'(\omega)$ (full line) and $G''(\omega)$ (broken line). The two maxima in G'' at $\omega=10^6$ and $\omega=10^9$ correspond to the entanglement contribution $(1/\tau_d)$ and the faster decaying compressibility contribution.

FIG. 4. The dynamic structure factor of the one-particle model, $C_{800}H_{1602}$ at 450 K (full lines) compared to the 12k system ($\approx C_{850}H_{1702}$) of Wischnewski et al. (Ref. 27) at 509 K (circles). The k values are from top to bottom: 0.3, 0.5, 0.77, and 1.15 nm^{-1}. Their combined Rouse-reptation fit is also shown (dotted lines).

found above. It is interesting to note that at intermediate times $G(t)$ deviates substantially from the two exponent representation. The reason for this is obviously the fact that the motion of the centers of mass of the polymers and the relaxation of the entanglement forces are strongly coupled to each other. In order to investigate this point further, we have plotted in Fig. 3 the storage and loss modulus,

$$G'(\omega) = \omega \int_0^\infty \sin(\omega t) G(t) dt,$$

$$G''(\omega) = \omega \int_0^\infty \cos(\omega t) G(t) dt. \qquad (17)$$

These have been obtained by a direct Fourier transform on the measured $G(t)$, where a exponential fit is used for the tail of $G(t)$ to lower the noise. Roughly speaking, $G''(\omega)$ may well be represented by the sum of two Maxwell peaks. At intermediate values of ω, however, i.e., in the valley between the two maxima, $G''(\omega)$ behaves rather differently from this representation. On the basis of the dashed line in Fig. 3, we argue that within statistical errors $G''(\omega)$ is roughly proportional to $\omega^{-0.25}$. A link to contour length fluctuations and constraint release (see Likhtman and McLeish[30]) is tempting. Actually, although the number of particles within the range of entanglement forces felt by a particular particle is large, fluctuations of this number are still substantial, resulting in a relaxation mechanism with some resemblance to contour length fluctuations and constraint release. Obviously, here, we just point at a striking resemblance in the data and do not provide a compelling argument. For the latter additional simulations with longer chains are needed.

Besides the shear relaxation modulus, a much studied dynamic property of a polymer melt is the single chain dynamic structure factor,
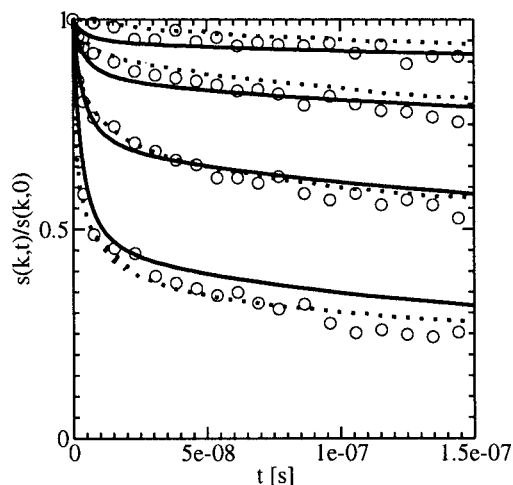
$$S(k,t) = \frac{1}{N_L} \left\langle \sum_i^{N_L} \sum_j^{N_L} \exp(i\mathbf{k} \cdot [\mathbf{r}_i(t) - \mathbf{r}_j(0)]) \right\rangle, \qquad (18)$$

where N_L is the number of scattering centers constituting the chain and $\mathbf{k}$ is the scattering vector. It provides information about the time evolution of the distribution of scattering centers. Roughly speaking, at small values of $k=|\mathbf{k}|$ only the movements of the chains as a whole are measured. With larger values of k, initially, the dynamics of the scattering distribution inside the chain is measured, while at later times also in this case mainly the diffusion of the chain as a whole is measured. An example of a single chain dynamic scattering function, measured[27] by means of a neutron-spin-echo experiment, is shown in Fig. 4. At all but the very low k values, $S(k,t)$ quickly decays at early times and then settles at a (very slowly decaying) plateau. At times beyond τ_e, $S(k,t)$ may be described by an expression first described by DeGennes[5] on the basis of the tube model, which in the notation of Wischnewski et al. reads

$$\frac{S(k,t)}{S(k,0)} = \{1 - \exp[-(kd/6)^2]\}S^{\text{loc}}(k,t)$$
$$+ \exp[-(kd/6)^2]S^{\text{esc}}(k,t). \qquad (19)$$

The functions $S^{\text{oc}}(k,t)$ and $S^{\text{esc}}(k,t)$ may be found in Ref. 27. The model parameter d is the so-called tube diameter. It is obtained from experimental data by adjusting its value until the difference between the theoretical and experimental data is minimal.

Obviously, from our single particle model we cannot obtain data related to the dynamics of the scattering distribution inside the chain, i.e., inside the particle. This is clear from a comparison of the experimental scattering functions and the ones obtained from our simulations for the largest k value in Fig. 4. (Note that the experimental system was slightly larger and at a slightly higher temperature than the simulated system. These two differences will have opposite effects on the comparison of experiment and simulation, which will there-
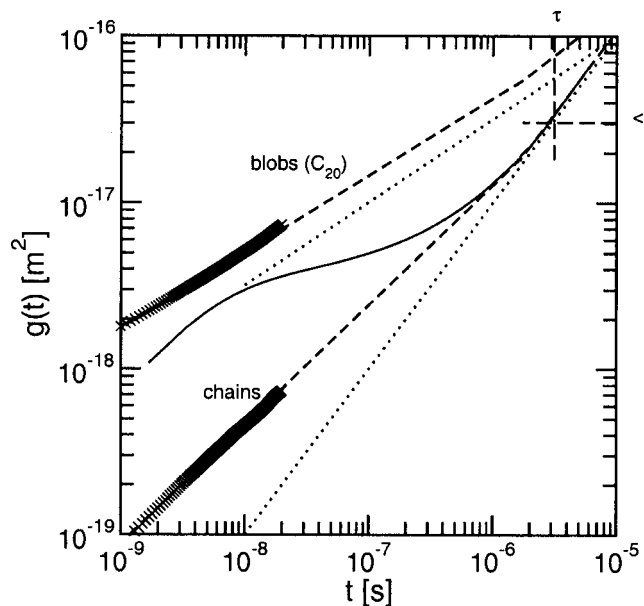
FIG. 5. The mean square displacement $g(t)$ of the system with (full line) entanglements. The two dotted lines represent $t^{1/2}$ and t^1. The latter is exactly equal to the results of the nonentangled system. Padding and Briels estimated that at τ_d the diffusion would reach R_G and become linear from there on in time. Their Twentanglement results of both the C_{20} blobs and their centers of mass are represented by the symbols and their long time extrapolation by the broken line. The diffusion coefficient of the entangled system, 1.5×10^{-12} m^2/s, is close to the experimental value of Pearson, 1.6×10^{-12} (Ref. 23).

fore partially cancel.) It is surprising, however, how similar the experimental and simulation curves are and how well they agree at the lower k values. It should be stressed, however, that the differences between the two at early times are substantial. The dotted line in Fig. 4 represents the fit on the experimental data by Wischnewski *et al.* using Eq. (19) with $d = 5.3$ nm. The qualitative agreement between the experimental data and the fit is much better than the agreement with our simulation results.

From the above discussion we infer that the early time diffusion of our particles is probably unrealistically fast. To investigate this point in more detail, we have plotted in Fig. 5 the mean square displacements of our particles,

$$g(t) = \langle (\mathbf{r}_i(t) - \mathbf{r}_i(0))^2 \rangle. \tag{20}$$

It is evident from the comparison with the data of Padding and Briels (the symbols) and their long time extrapolation (the broken lines) that at the very early times our particles move too fast and consequently slow down too fast. This is inherent in the use of a Brownian propagator with relatively small frictions. Only at times beyond 10^{-7} s, the mean square displacements of the centers of mass of the polymers are represented reasonably well by our model. Note that the error made at earlier times in absolute value is very small and therefore hardly noticeable in the plot of the $S(q,t)$.

D. Unentangled dynamics

To understand the importance of the entanglement forces we investigate the same system as above, but now without

entanglements. Besides removing the entanglement contributions from the forces, we must also redefine the frictions,

$$\xi_i = \xi_0. \tag{21}$$

This constant background friction is tuned to obtain the correct diffusion. Taking $\xi_0 = 13$ aJ/ns results in the mean square displacements represented in Fig. 5 by the dashed line. As a result of the simplicity of the model, this is a straight line at all times, with a corresponding diffusion coefficient $D = 1.5 \times 10^{-12}$ m^2/s. Since the friction in this case is adjusted to the long time dynamics, the mean square displacements at early times are much smaller than those of the entangled model, having an average friction $\langle \xi_i \rangle \approx 3 - 5$ aJ/ns.

Since the only free parameter in the present model, i.e., the simple Brownian dynamics model without entanglements, has been adjusted to obtained the desired diffusion coefficient, the viscosity cannot be set *a priori* and will be a prediction of the model. Calculating the viscosity, we found $\eta = 0.09$ Pa s i.e., two orders of magnitude smaller than the experimental value, which was well reproduced with the entangled model. A closer look at the shear relaxation modulus $G(t)$ revealed that it decays according to a single exponent, in marked contrast to the decay of $G(t)$ in the entangled model. Similarly, the unentangled $S(k,t)$ differs qualitatively and quantitatively from that in the entangled system.

The results in this section show that the introduction of entanglements in a single particle description of a polymer chain is necessary to qualitatively and quantitatively describe the dynamics of a polymer melt. Since the presence of entanglements does not influence the static properties of the system, the latter may be reproduced by using the correct potential of mean force. Here, we show that a very simple version of MDPD is sufficiently accurate.

IV. TRANSIENT AND STEADY STATE SHEAR

A. Setup

An important feature of polymer melts is their strong shear thinning behavior. From an industrial point of view, the relevance of understanding shear thinning is enormous if only because in molding processes the melt is subjected to high shear rates. Substantial efforts have been made to describe and understand the underlying physical elements.[6,8,9,31] Since the tube theory of Doi and Edwards overpredicts shear thinning, several additional relaxation mechanisms, for example, CR and CCR (Ref. 7) have been proposed. Similar relaxation mechanisms to these are operational in our very coarse model. While entanglement forces, just like the tube, tend to conserve existing structures, fluctuations of the environment and flow gradients give rise to constraint release. To investigate these points a bit further we now study transient and steady state effects after startup of shear flow.

In order to simulate shear flow, a term,

$$\mathbf{u}(\mathbf{r}_i)dt = r_{y,i}\dot{\gamma}\hat{\mathbf{e}}_x, \tag{22}$$

must be added on the right hand side of Eq. (3). Here, $r_{y,i}$ is the y coordinate of $\mathbf{r}_i$ and $\dot{\gamma}$ is the imposed shear rate. Appropriate boundary conditions are the standard Lees-
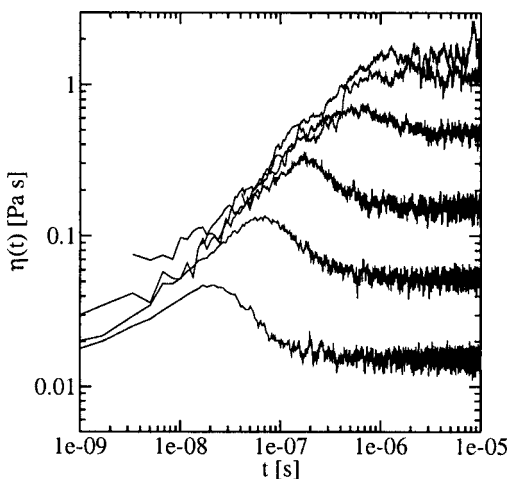
FIG. 6. The transient viscosity for different shear rates as a function of time. From top to bottom $\dot{\gamma}$ is $0.1\tau_d^{-1}$, $0.3\tau_d^{-1}$, $1\tau_d^{-1}$, $3\tau_d^{-1}$, $10\tau_d^{-1}$, $30\tau_d^{-1}$, and $100\tau_d^{-1}$. The lower shear rates grow slowly to the final viscosity, while all shear rates above τ_d^{-1} show an overshoot that increases with increasing $\dot{\gamma}$. The strain at which the overshoot takes place increases as well, in agreement with the extended tube theories.

FIG. 7. The strain dependent overshoot in the transient viscosity for shear rates above τ_d^{-1}. $\dot{\gamma}=10\tau_d^{-1}$ is represented by the full line, 30 by the dotted line, and 100 by the broken line. The increase in the strain at which the maximum occurs is qualitatively in agreement with experiments and theory (Ref. 34) but differs in value by a factor of 2. On this scale the increase in the relative overshoot is also clearly visible.

Edwards boundary conditions.[32] We have tested the assumption, inherent in the use of Eq. (22), that the linear flow field is the most stable flow field by performing a series of duplicate runs with variable flow fields. In these runs $\mathbf{u}(\mathbf{r}_i)dt$ was taken to be the average displacement of particles in a slab with the y coordinate equal to $r_{y,i}$. In all these tests, over a wide range of values of $\dot{\gamma}$, the resulting flow field was linear.

B. Transient shear flow

To study the transient response of our model we investigated the time evolution of the viscosity $\eta(t)$ and the first normal stress difference $\Psi_1(t)$ after the onset of shear flow in a well equilibrated system at $t=0$,

$$\eta(t) = \frac{\sigma_{xy}(t)}{\dot{\gamma}}, \qquad (23)$$

$$\Psi_1(t) = \frac{\sigma_{xx}(t) - \sigma_{yy}(t)}{\dot{\gamma}^2}. \qquad (24)$$

Figure 6 shows the normalized transient viscosity $\eta(t)/\eta$ for six different values of $\dot{\gamma}$, both below and above $\dot{\tau}_d^{-1}$. For shear rates below τ_d^{-1} the stresses grow monotonously to their final values. At higher shear rates overshoots appear, i.e., stresses reach a maximum at some value of strain before dropping to their final value. The overshoot and the strain at which this occurs increase with increasing $\dot{\gamma}$, which is in agreement with theories including CR/CCR and with experiments.[11,33,34] The maximum overshoots occur at strains between 1.1 and 1.3, as can be seen in Fig. 7. These values are somewhat smaller than the corresponding experimental values, which are near strains equal to about 2. In Fig. 8 it is shown that it is mainly the entanglement forces which are responsible for the overshoots and that the contributions of the compressibility forces to the stress are negligible.

In Fig. 9 we present the first normal stress difference $\Psi_1(t)$ for four values of $\dot{\gamma}$. Again, overshoots appear, but this
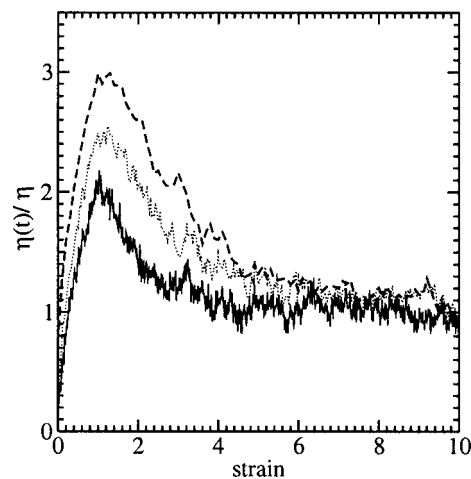
time somewhat weaker than those in the transient viscosity. The relative overshoot for the largest $\dot{\gamma}$ studied is 2.5, whereas the corresponding overshoot for $\eta(t)$ was larger than 3. The strain at which $\Psi_1(t)$ reaches its maximum is about twice as large as the strain where $\eta(t)$ reaches its maximum. Finally, we notice that the shear rate needed to develop overshoots is somewhat larger in the case of first normal stress differences than in the case of shear viscosities, as may be inferred from comparing the cases with $\dot{\gamma}=3\tau_d^{-1}$ in Figs. 6 and 9. All these findings are qualitatively in agreement with those of previous simulations[25] and with experiments and theory.[11,34]

In the extended tube model, the existing tubes and chains at time zero are stretched after the shearing motion has been imposed. This leads to a substantial increase of stresses in the system. At the same time stretched chains start to retract in their deformed tubes, thereby lowering the stresses. In case the characteristic time for retraction is small compared
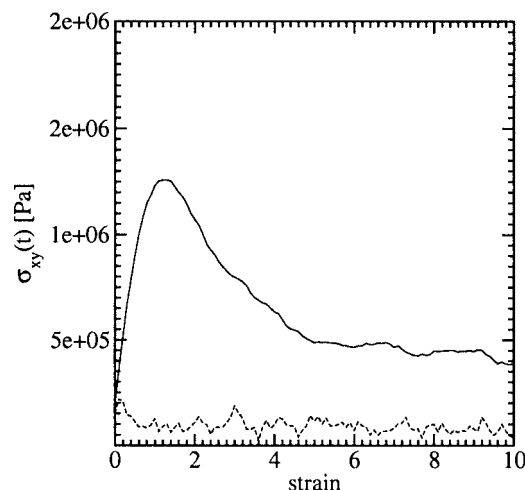

FIG. 8. The contribution of the entanglements (full line) and of the compressibility (broken line) to the total stress during the startup of shear as a function of the applied strain. The shear rate is $10^2\tau_d^{-1}$.
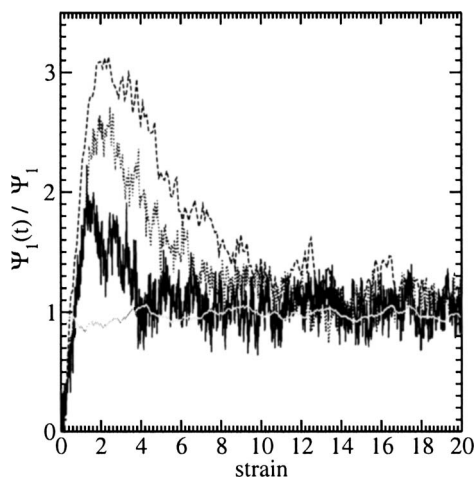
FIG. 9. The strain dependent overshoot in the transient first normal stress difference Ψ_1 for shear rates above τ_d^{-1}. $\dot{\gamma}=3\,\tau_d^{-1}$ is represented by the gray line, 10 by the full line, 30 by the dotted line, and 100 by the broken line. The data for $\dot{\gamma}=3\,\tau_d^{-1}$ are running averages to reduce the noise and increase the readability of the graph. The overshoot starts at higher shear rates and is located at roughly twice the strain of the maxima in the overshoots in the viscosity (Fig. 7).

FIG. 10. The flow curve, η vs $\dot{\gamma}$. The solid line is extracted from the equilibrium simulation via the Cox-Merz rule [Eq. (25)]; the circles (linear background) and the squares (variable flow field) are measured in shear with Eq. (23).

to $1/\dot{\gamma}$, deformation will gradually grow until the deformation rate and the rate of retraction are balanced. At this time stresses have reached their maximum and final value. In the opposite case the deformation of the chains and the development of stresses will reach a maximum before chain retraction becomes effective and lowers the stress until the deformation and retraction rate are balanced again and the stress reaches its final value.

In our model of spherical particles the tube concept has no meaning. Similar to the tube, however, our entanglement forces tend to resist deformation of the current configuration. After onset of shearing flow, therefore, the contribution of the entanglement forces to the stress increases quickly. At the same time the relaxation of the entanglement numbers toward their equilibrium values tries to lower the stress. In case the characteristic time τ of this process is much smaller than $1/\dot{\gamma}$, the number of entanglements and corresponding stress gradually grow until they reach their final values. In case τ is larger than $1/\dot{\gamma}$ the entanglement contribution to the stress quickly grows until the flow has completely destroyed the original configuration. After this time each particle must develop entanglements with its new environment. The average number of entanglements then depends on the relative values of the characteristic time τ and the time $1/\dot{\gamma}$ given to each particle to develop entanglements. The corresponding average stress may well be smaller than the stress generated by the equilibrium distribution of entanglement numbers in a highly deformed structure. This then leads to a lowering of the stress after a strain of about 1 has been reached, as found in Figs. 6–9.

C. Steady state shear flow

In Fig. 10 we have plotted viscosities against shear rate. Circles refer to simulations with an imposed background flow as in Eq. (22). Squares are obtained with a propagator in which Eq. (2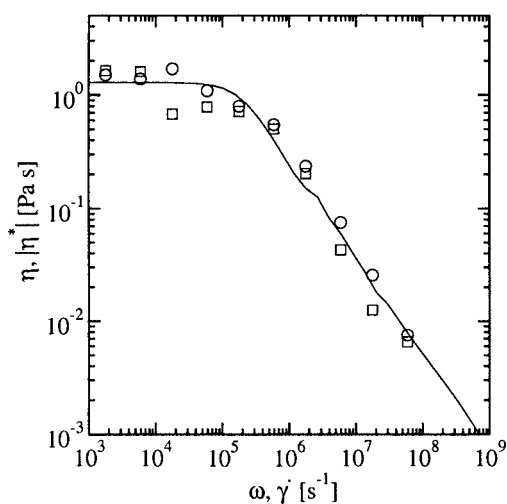2) has been replaced by the average displace-ment $\langle d\mathbf{r}_i \rangle$ of all particles in the slab to which particle i belongs. In the latter case, the flow has the freedom to shear band. Within statistical errors, however, both methods give the same results, indicating that no tendency for banding exists. We have checked the latter by inspection of the flow fields.

In the limit of small shear rates the viscosity approaches 1.5 Pa s, equal to the result obtained from the equilibrium simulation discussed in the previous section. Beyond shear rates of about $1/\tau$ the system starts to shear thin, as might also have been inferred from the stationary values of the viscosities shown in Fig. 6. Shear thinning is as strong as $\eta \propto \dot{\gamma}^{-1}$. The reason for this behavior is not difficult to understand. At low shear rates entanglement forces and potential forces increase linearly with imposed deformation rates, leading to shear rate independent viscosities. For shear rates larger than about $1/\tau$, particles hardly have time to develop entanglements with their neighbors before the flow has advected them to new environments. As a result, the contribution of entanglement forces to the stress becomes constant, i.e., independent of shear rate. Since the entanglement forces constitute the dominant contribution to the stress, the latter becomes independent of $\dot{\gamma}$ as well and the viscosity becomes proportional to $\dot{\gamma}^{-1}$. Only after the contributions of the potential forces to the stress have grown enough to outweigh the contributions of the entanglement forces will the stress start to increase again and the viscosity becomes constant.

In the literature, slopes of $\ln \eta$ vs $\ln \dot{\gamma}$ in the shear thinning regime have been reported in the range of -1 to -0.5.[35–43] Recent work of Vega et al.[41] has shown that high molecular weight monodisperse polyethylene melts shear thin as $\eta \propto \dot{\gamma}^{-1}$. It seems reasonable to conclude that this holds true for all monodisperse melts of very long chains. Recent work of Teixeira et al. shows the slope of -1 in heavily entangled DNA solutions as well.[43] Polydispersity and strong dilution of chains might lead to less pronounced shear thinning curves, possibly due to the introduction of new relaxation mechanisms or to unnoticed shear
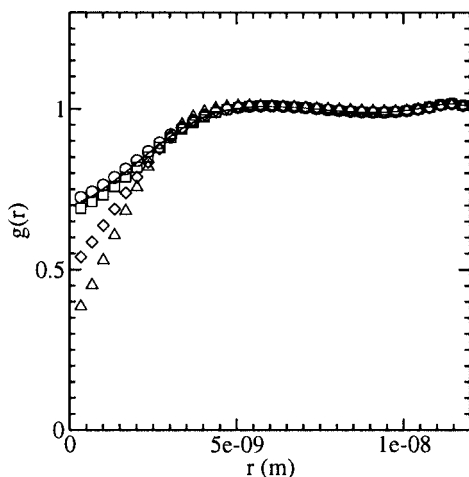
FIG. 11. The $g(r)$ as a function of $\dot{\gamma}$. Expressed in τ_d^{-1}, the shear rates are 10^{-2} (full line), 10^{-1} (circles), 10^0 (squares), 10^1 (diamonds), and 10^2 (triangles).

banding.[44,45] Melts of shorter chains also have less pronounced shear thinning probably because the relaxation spectrum is not yet dominated by very long times. In our model the spectrum of relaxations is more or less bimodal, with the relaxation caused by potential forces at short times and those caused by entanglement forces at long times. Although being applied here to relative short chains, our results therefore resemble those of long chains more than those of short chains.

Figure 10 contains one more piece of information, which we have not yet discussed. The drawn line in this figure has been obtained by applying the Cox-Merz rule to the linear data of the previous section. To be concrete, the drawn line represents $|\eta^*(\dot{\gamma})|$ with

$$\eta^*(\omega) = \int_0^\infty \exp(-i\omega t)G(t)dt. \qquad (25)$$

Just like with experimental polymer melts, it is seen that with our model the Cox-Merz rule holds true very well.

Finally, in Fig. 11, we have plotted radial distribution functions for various sheared systems. It is seen that with increasing shear rate, the correlation hole near $r=0$ becomes more and more pronounced. The origin of this behavior is to be found in the entanglement forces. For shear rates larger than $1/\tau$, a pair of particles hardly develop entanglements before the flow has separated them again. This leads to strong repulsive forces pushing the particles to larger distances along the gradient direction.

V. CONCLUSIONS AND DISCUSSION

Given the complexity of continuous descriptions of polymer melts in flow in complex geometries, using realistic rheological constitutive equations, we have thought it worthwhile to derive a particle based coarse grain model of polymer melts in which each polymer chain is represented as just one particle. With this model, we have been able to qualitatively, and to a large extent quantitatively, reproduce the static as well as the dynamic properties of a typical polymer melt.

Coarse graining static and thermodynamic properties of polymer melts, and soft matter in general, invariably leads to soft interactions governed by soft potentials of mean force. Every dynamic model based on such a potential and ignoring memory effects is deemed to produce large viscosities combined with small diffusion coefficients or small viscosities with large diffusion coefficients. It will be impossible with such a model to reproduce large viscosities combined with large diffusion coefficients, which is typical for polymer melts. Here, we have chosen to refrain from using hard potentials, derived from a realistic representation of the free energy, and to incorporate memory into the model by introducing a restricted set of parameters describing the deviation from the equilibrium of the ignored coordinates. The dynamics of these new parameters have been devised such that they do not influence the static or thermodynamic properties of the system as a whole. The new degrees of freedom that we have introduced are the numbers of entanglements n_{ij} for each pair of chains i and j. The fluctuations of these numbers around their equilibrium values give rise to additional elastic forces, which are responsible for most of the rheological properties of our model.

We have applied our model to a polyethylene melt of $C_{800}H_{1602}$ molecules. Our findings may be summarized as follows.

- It is possible to have an almost ideal gaslike structure for the centers of mass of the polymers, and still reproduce the right compressibility.

- It is possible to tune the two parameters in our model such as to reproduce large viscosities combined with large diffusion coefficients.

- The single particle dynamic scattering function $S(q,t)$ may be reproduced qualitatively and, to some extent, quantitatively as well.

- The shear relaxation modulus $G(t)$ may be reproduced qualitatively and, to a good extent, quantitatively as well; the corresponding $G'(\omega)$ and $G''(\omega)$ show several features which are characteristic of polymer melts and which are usually explained in terms of tube concepts; additional simulations with much longer chains are needed before any claims can be laid with respect to the interpretation of the details of these functions.

- Startup effects after the onset of shear flow are in good agreement with experiments.

- Flow curves with strong shear thinning are reproduced; no tendency to shear banding is observed.

Of course, it is not be expected that a model as coarse as the one presented in this paper can quantitatively reproduce all features of a polymer melt. It is pleasing, however, that our model so far never failed to be in qualitative agreement with experiments. We think that it is possible to increase quantitative agreement a bit by decorating the model with additional features. For example, by introducing the possibility for the molecules to deform under entanglement forces, it

should be easy to make overshoots after the onset of shear occur at a strain of about 2 instead of 1, as with the present model.

This model can play an important role in particle based simulations that require viscoelastic properties of a system. In simulations of viscoelastic phase separation the model might be used to study effects such as phase inversion. In the field of colloid simulations the large time step is very welcome. Colloids dissolved in a viscoelastic medium cannot be simulated with traditional particle based simulation methods due to the large separation of time and length scales of the colloids compared to atoms or chain segments. The high level of coarse graining of the proposed model overcomes these problems while conserving the most important melt properties. We will use this model in future work to investigate diblock copolymers in shear flow.

ACKNOWLEDGMENTS

APPENDIX A: DERIVATION OF THE INCOMPRESSIBILITY FORCE

To derive a conservative force that incorporates the correct compressibility, we take the free energy A_c to be a sum of the free energy per particle a, each being a function of a local density ρ_i,

$$A_c[\rho] = \sum_{i=1}^{N} a_c(\rho_i) = \sum_{i=1}^{N} a_c(\rho + \Delta_i)$$
$$= \sum_{i=1}^{N} a_c(\rho) + \sum_{i=1}^{N} a_c'(\rho)\Delta_i + \frac{1}{2}\sum_{i=1}^{N} a_c''(\rho)\Delta_i^2$$
$$+ \cdots, \qquad (A1)$$

where Δ_i is the local deviation from the global density $\rho = N/V$ and primes denote derivatives with respect to ρ. From thermodynamics we have

$$a_c'(\rho) = \frac{P}{\rho^2}$$
$$a_c''(\rho) = \frac{1}{\rho^3}\left(\frac{1}{\kappa_T} - 2P\right), \qquad (A2)$$

where P is the pressure and κ_T the isothermal compressibility. The local density around each particle is defined as a sum of normalized weight functions $\omega(r_{ij})$ of the neighboring particles j,

$$\rho_i = \sum_j \omega(r_{ij}),$$
$$\qquad (A3)$$
$$\Delta_i = \sum_j \omega(r_{ij}) - \rho.$$

The resulting force on particle i can now be expressed in terms of the positions of the surrounding particles,

$$\mathbf{F}_i = -\nabla_i A_c[\rho] = -\frac{P}{\rho^2}\nabla_i \sum_{j=1}^{N}\sum_{k=1}^{N}\omega(r_{jk})$$
$$-\sum_{j=1}^{N}\frac{1}{\rho^3}\left(\frac{1}{\kappa_T} - 2P\right)\Delta_j\nabla_i\sum_{k=1}^{N}\omega(r_{jk})$$
$$= -\frac{2P}{\rho^2}\sum_{j=1}^{N}\nabla_i\omega(r_{ij}) - \frac{1}{\rho^3}\left(\frac{1}{\kappa_T} - 2P\right)$$
$$\times \sum_{j=1}^{N}\Delta_j\nabla_i\omega(r_{ij})$$
$$-\frac{1}{\rho^3}\left(\frac{1}{\kappa_T} - 2P\right)\sum_{j=1}^{N}\Delta_i\nabla_i\omega(r_{ij})$$
$$= \frac{2P}{\rho^3}\sum_{j=1}^{N}(\Delta_j + \Delta_i - \rho)\nabla_i\omega(r_{ij})$$
$$-\frac{1}{\rho^3\kappa_T}\sum_{j=1}^{N}(\Delta_j + \Delta_i)\nabla_i\omega(r_{ij}). \qquad (A4)$$

Although the force is derived from a multibody approach, the outcome is a pairwise force, which is a pleasant side effect to reduce simulation time. The first term in the last line of Eq. (A4) is negligible compared to the second since $2P$ (10^5 Pa) is orders of magnitude smaller than κ_T^{-1} (10^9 Pa). Thus, we implemented

$$\mathbf{F}_i = -\frac{1}{\rho^3\kappa_T}\sum_{j=1}^{N}(\Delta_j + \Delta_i)\nabla_i\omega(r_{ij}) = -\nabla_i\left[\frac{1}{2\rho^3\kappa_T}\sum_j \Delta_j^2\right].$$
$$\qquad (A5)$$

[1] W. Paul, G. D. Smith, D. Y. Yoon, B. Farago, S. Rathgeber, A. Zirkel, L. Willner, and D. Richter, Phys. Rev. Lett. **80**, 2346 (1998).
[2] D. Richter, M. Monkenbusch, A. Arbe, J. Colmenero, B. Farago, and R. Faust, J. Phys.: Condens. Matter **11**, A297 (1999).
[3] D. Richter, M. Monkenbusch, J. Allgeier, A. Arbe, J. Colmenero, B. Farago, Y. C. Bae, and R. Faust, J. Chem. Phys. **111**, 6107 (1999).
[4] P. E. Rouse, J. Chem. Phys. **21**, 1272 (1953).
[5] P. G. DeGennes, J. Phys. (Paris) **42**, 735 (1981).
[6] M. Doi and S. F. Edwards, *The Theory of Polymer Dynamics* (Oxford Science, Oxford, 1986).
[7] G. Marrucci, J. Polym. Sci., Polym. Phys. Ed. **23**, 159 (1985).
[8] G. Marrucci, J. Non-Newtonian Fluid Mech. **62**, 279 (1996).
[9] A. E. Likhtman, S. T. Milner, and T. C. B. McLeish, Phys. Rev. Lett. **85**, 4550 (2000).
[10] T. C. B. McLeish, Adv. Phys. **51**, 1379 (2002).
[11] R. S. Graham, A. E. Likhtman, and T. C. B. McLeish, J. Rheol. **47**, 1171 (2003).
[12] J. T. Padding and W. J. Briels, J. Chem. Phys. **114**, 8685 (2001).
[13] V. A. Harmandaris, V. G. Mavrantzas, D. N. Theodorou, M. Kroger, J. Ramirez, H. C. Ottinger, and D. Vlassopoulos, Macromolecules **36**, 1376 (2003).
[14] J. T. Padding and W. J. Briels, J. Chem. Phys. **115**, 2846 (2001).
[15] W. Paul, K. Binder, D. W. Heermann, and K. Kremer, J. Chem. Phys. **95**, 7726 (1991).
[16] K. Kremer and G. S. Grest, J. Chem. Phys. **92**, 5057 (1990).
[17] M. Murat, G. S. Grest, and K. Kremer, Europhys. Lett. **42**, 401 (1998).
[18] A. van den Noort, W. K. den Otter, and W. J. Briels, EPL **80**, 28003 (2007).

[19] W. J. Briels, *Theory of Polymer Dynamics, Lecture Notes* (Uppsala University, Uppsala, 1994), (The full text can be downloaded from http://cpb.tnw.utwente.nl/polymeerdictaat/).

[20] I. Pagonabarraga and D. Frenkel, Mol. Simul. **25**, 167 (2000).

[21] I. Pagonabarraga and D. Frenkel, J. Chem. Phys. **115**, 5015 (2001).

[22] S. Y. Trofimov, E. L. F. Nies, and M. A. J. Michels, J. Chem. Phys. **117**, 9383 (2002).

[23] D. S. Pearson, G. Ver Strate, E. von Meerwall, and F. C. Schilling, Macromolecules **20**, 1133 (1987).

[24] J. T. Padding and W. J. Briels, J. Chem. Phys. **117**, 925 (2002).

[25] J. T. Padding and W. J. Briels, J. Chem. Phys. **118**, 10276 (2003).

[26] J. T. Padding and W. J. Briels, J. Chem. Phys. **120**, 2996 (2004).

[27] A. Wischnewski, M. Monkenbusch, L. Willner, D. Richter, A. E. Likhtman, T. C. B. McLeish, and B. Farago, Phys. Rev. Lett. **88**, 058301 (2002).

[28] V. G. Mavrantzas, T. D. Boone, E. Zervopoulou, and D. N. Theodorou, Macromolecules **32**, 5072 (1999).

[29] H. H. Rugh, Phys. Rev. Lett. **78**, 772 (1997).

[30] A. E. Likhtman and T. C. B. McLeish, Macromolecules **35**, 6332 (2002).

[31] D. W. Mead, R. G. Larson, and M. Doi, Macromolecules **31**, 7895 (1998).

[32] M. P. Allen and D. J. Tildesley, *Computer Simulations of Liquids* (Clarendon, Oxford, 1987).

[33] C. C. Hua and J. D. Schieber, J. Chem. Phys. **109**, 10018 (1998).

[34] C. C. Hua, J. D. Schieber, and D. C. Venerus, J. Rheol. **43**, 701 (1999).

[35] W. Graessley, J. Chem. Phys. **47**, 1942 (1967).

[36] M. M. Cross, J. Appl. Polym. Sci. **13**, 765 (1969).

[37] M. M. Cross, Rheol. Acta **18**, 609 (1979).

[38] W. M. Kulicke and R. S. Porter, Rheol. Acta **19**, 601 (1980).

[39] S. T. Milner, J. Rheol. **40**, 303 (1996).

[40] C. Y. Liu, J. Wang, and J. S. He, Polymer **43**, 3811 (2002).

[41] J. F. Vega, S. Rastogi, G. W. M. Peters, and H. E. H. Meijer, J. Rheol. **48**, 663 (2004).

[42] X. N. Ye and T. Sridhar, Macromolecules **38**, 3442 (2005).

[43] R. E. Teixeira, A. K. Dambal, D. H. Richter, E. S. G. Shaqfeh, and S. Chu, Macromolecules **40**, 2461 (2007).

[44] P. Tapadia and S. Q. Wang, Phys. Rev. Lett. **96**, 016001 (2006).

[45] P. Tapadia, S. Ravindranath, and S. Q. Wang, Phys. Rev. Lett. **96**, 196001 (2006).

[46] *Handbook of Chemistry and Physics*, 5th ed., edited by R. C. Weast (CRC, Boca Raton, FL, 1996).